photonics

MDPI

Article

An InGaAs Vertical-Cavity Surface-Emitting Laser Emitting at 1130 nm for Silicon Photonics Application

Yunfeng Fang [1,2], Yang Zhang [1,2,*], Chuanchuan Li [1,2], Jian Li [1,2], Yongli Wang [1,2] and Xin Wei [1,2,*]

[1] Laboratory of Nano Optoelectronics, Institute of Semiconductors, Chinese Academy of Sciences, Beijing 100083, China; yffang@semi.ac.cn (Y.F.); lichuan@semi.ac.cn (C.L.); jalain@semi.ac.cn (J.L.); wangyongli@semi.ac.cn (Y.W.)
[2] College of Materials Science and Optoelectronic Technology, University of Chinese Academy of Sciences, Beijing 100049, China
* Correspondence: zhangyang@semi.ac.cn (Y.Z.); weix@semi.ac.cn (X.W.)

Abstract: A highly strained InGaAs quantum well (QW) vertical-cavity surface-emitting laser (VCSEL) with low threshold current density, high efficiency and output power emissions around 1130 nm was grown by MOCVD. Its static characteristics at room temperature and high operation temperature were studied in detail. The 7 µm oxide aperture device exhibits a threshold current of 0.68 mA, corresponding to a threshold current density of 1.7 kA/cm^2. The slope efficiency is 0.43 W/A and the maximum output power is 3.3 mW. Continuous-wave (CW) operation in the 10–80 °C temperature range is observed. The slope efficiency is almost constant at 10–80 °C. The threshold current becomes lower at high temperatures thanks to the alignment between gain peak and cavity mode. The 3 µm oxide aperture device's lasing in single mode with the RMS spectral width of 0.163 nm and orthogonal polarization suppression ratio (OPSR) is ~15 dB at 25 °C. The small-signal response analysis indicates that reducing the parasitics of the device and refining the fabrication process will improve the dynamics response characteristics. These results indicate that the 1130 nm GaAs-based VCSEL with highly strained InGaAs QWs is expected to be used as source for silicon photonics.

Keywords: highly strained; InGaAs quantum wells; VCSEL; output characteristics

check for updates

Citation: Fang, Y.; Zhang, Y.; Li, C.; Li, J.; Wang, Y.; Wei, X. An InGaAs Vertical-Cavity Surface-Emitting Laser Emitting at 1130 nm for Silicon Photonics Application. *Photonics* **2024**, *11*, 207. https://doi.org/10.3390/photonics11030207

Received: 3 January 2024
Revised: 3 February 2024
Accepted: 5 February 2024
Published: 26 February 2024

1. Introduction

With the emerging trend of big data, Internet of Things and 5G, there is increasing demand for high-capacity data links. The total global traffic volume in 2030 is predicted to be 5016 Exabit/month, where 2020 was 62 Exabit/month [1].

Optical interconnects promise higher communication speeds and lower signal attenuation than electrical interconnects. Due to their advantages of compact size, cost-effectiveness and power-efficiency, photonic integration technology has been commercialized recently. Silicon photonics has become one of the most suitable integrated optical platforms due to the ability to use complementary metal oxide semiconductor (CMOS)-compatible facilities. In the platform of silicon photonics, various photonic components have been demonstrated, such as modulators [2–4], (de)multiplexers [5–8] and photodetectors [9,10]. The lack of a reliable silicon laser has been the major impediment due to silicon's indirect bandgap.

Various heterogeneous integrations of lasers on silicon have been demonstrated [11]. However, these devices should operate at a small voltage and current, have a small footprint and be cost-effective. In addition, for efficiently coupling and transmitting in Si waveguides, the lasers should operate above 1.1 µm.

VCSELs have shown the advantages of power efficiency and a circular symmetry output beam with small divergence angle, and can be mass fabricated and on-wafer tested at low cost. Short-reach optical interconnects employing GaAs-based VCSELs dominate today's data centers and high-performance computing systems. Since 850 nm GaAs-based VCSELs are not compatible with silicon, long-wavelength-band InP-based VCSELs suffer from material and heat extraction, and the scalability of VCSELs is limited. Aside from these materials, a highly strained InGaAs/GaAs QW is also a candidate, which has an emitting range covering 1.1 µm. However, the problems in highly strained InGaAs/GaAs QW materials are an increase in QW roughness and the introduction of defects due to difficulty in epitaxial growth. At present, a few papers have reported VCSELs with highly strained InGaAs QWs emitting at 1.1 µm range and push this limit considerably. In 2002, the Koyama group at Tokyo Institute of Technology demonstrated highly strained GaInAs/GaAs QW VCSELs emitting at 1.16 µm [12]. The threshold current of the 10 µm current aperture device is 3 mA, corresponding to a threshold current density of 3 kA/cm^2. It has a maximum output power of more than 2 mW and a slope efficiency of 0.3 W/A at 25 °C. In 2006, Grenouillet et al. developed GaAs-based VCSELs emitting in the 1.1–1.3 µm range with GaInAs/GaAs or GaInNAs/GaAs QWs as the active materials [13]. The results show that nitrogen incorporation induces non-radiative defects in the active material together with an increase in the alloy disorder, and therefore results in an increase in the threshold current density and a poorer temperature stability. They improved the structure of the GaInAs VCSEL and the 10 µm aperture device shows a threshold current of 0.9 mA (threshold current density of 1.1 kA/cm^2) and a maximum output power of 1.52 mW. They also developed a single QW VCSEL (7 µm oxide aperture diameter), of which the threshold current is 120 µA, which corresponds to a threshold current density of 312 A/cm^2. The maximum output power is 0.93 mW. In 2008, Stevens et al. presented long-wavelength (1.1 µm) single-mode micro-structured photonic crystal strained InGaAs quantum well VCSELs [14]. The epitaxial structure was grown by Molecular Beam Epitaxy (MBE). The micro-structured 50 µm diameter mesa VCSELs with 10 µm oxidation aperture exhibited more than 1 mW optical power, 2 to 5 mA threshold currents and more than 30 dB side mode suppression ratio (SMSR) at a wavelength of 1090 nm. A lower threshold current density is favorable for high-temperature operation and practical application. Moreover, several QWs are also needed to support high output power. In this paper, we developed a highly strained InGaAs/GaAs QW VCSEL with low-threshold and high-output characteristics emitting at 1130 nm range.

2. VCSEL Design and Fabrication

The 1130 nm VCSEL was grown on an n^+-GaAs substrate by an AIXTRON 2800G4 metalorganic chemical vapor deposition (MOCVD) system. The gas sources included trimethylgallium (TMGa), trimethylindium (TMIn) and trimethylaluminium (TMAl). Arsine (AsH_3) was used as the hydride gas, and hydrogen was used as the carrier gas to deliver the MO precursors. Disilane (Si_2H_6) and carbontetrabromide (CBr_4) were used as dopant sources. The growth temperature range and pressure range were 630–720 °C and 20–100 mbar, respectively. The bottom distributed Bragg reflector (DBR) consisted of 41 pairs of Si-doped AlAs/GaAs layers and 5 pairs of Si-doped $Al_{0.9}GaAs/Al_{0.12}GaAs$ layers. The AlAs/GaAs layers were beneficial for heat dissipation. The reflectivity of 46 n-DBR pairs was over 99.9%. The active region consisted of strained InGaAs/GaAs QWs. The thickness of the InGaAs well layer and GaAs barrier layer was 4 nm and 8 nm, respectively. The In content in the QW was 38%. Above the active region was a p-DBR stack, and the transverse optical and current confinement were provided by an AlAs layer after wet oxidation. For series resistance reduction purposes, intermediate composition layers were inserted between the gallium-rich and aluminum-rich layers, and δ-doping was introduced at the interfaces. The longitudinal optical confinement was a 1 λ thick cavity. By adjusting the separate confinement layer thickness, the QWs were exactly positioned at the antinode of the optical standing wave.

The VCSEL fabrication process started with various diameter mesas defined by inductively coupled plasma (ICP) dry etching. The etch conditions were 500 W ICP, 15 sccm Cl_2, 45 sccm BCl_3 and 4 mTorr pressure. After ICP dry etching, the wafer was sent to an oxidation furnace to oxidize the AlAs layer in the p-DBR, which laterally confines current and optical field. The high temperature accuracy of the oxidation furnace is

±0.5 °C, and we used a pre-run wafer to accurately adjust the oxidation conditions before each process, which reduced the influence of the environment. Therefore, the oxidation depth was precisely controlled during the wet oxidation process. After the oxidation process, we determined the oxidation depth by an infrared ccd camera and the results were confirmed by a focused-ion-beam (FIB) process. Then, the P-type Ti/Pt/Au metal contact was sputtered on top of the p-DBR.

After thinning the substrate, an n-type AuGe/Ni/Au metal contact was evaporated on the back of the substrate. The contacts were thermally annealed to form ohmic contacts. Figure 1a–c show the schematic structure, side view scanning electron microscopy (SEM) image and top view of the fabricated 1130 nm VCSEL, respectively.

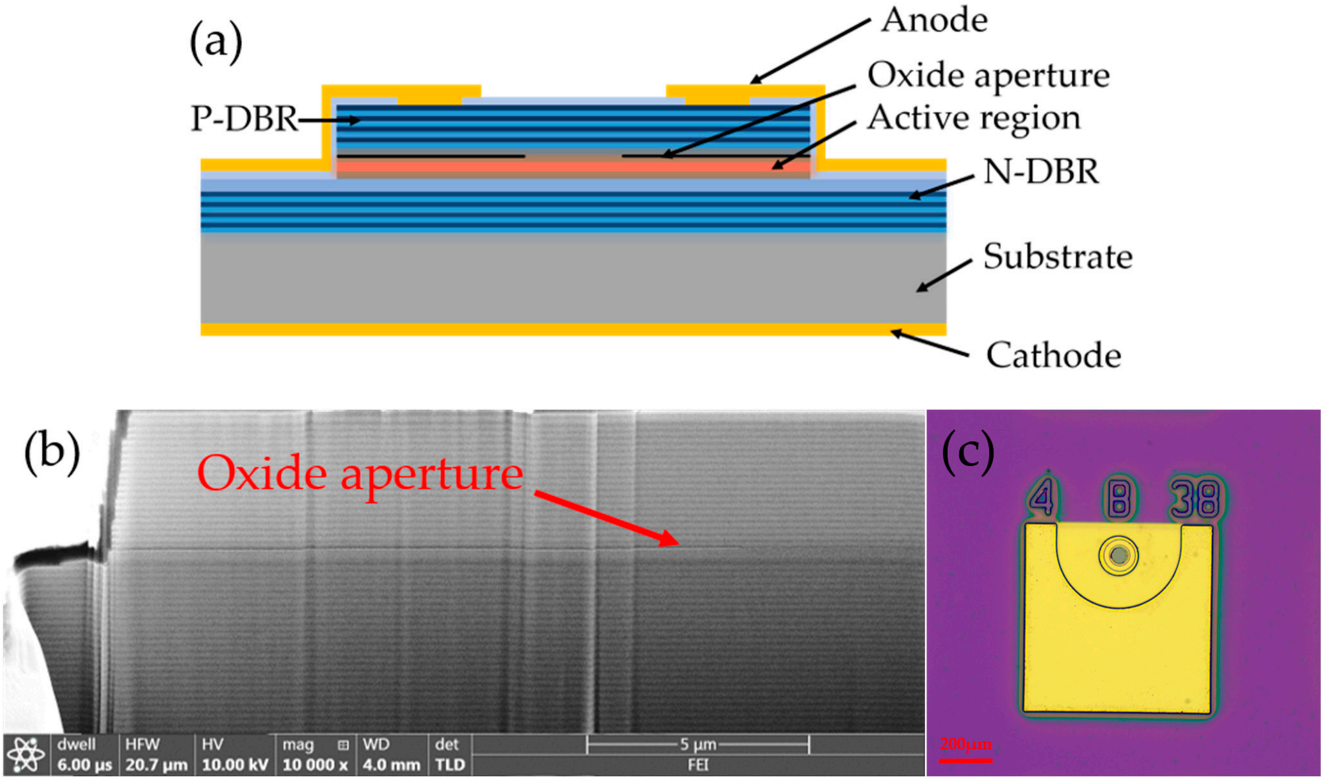

Figure 1. (**a**) Schematic cross-section of VCSEL structure; (**b**) SEM image of the cross-section of the device; (**c**) top view of fabricated VCSEL.

3. VCSEL Static Characteristics

The VCSELs were placed on a heatsink and the temperature was controlled. The measured Power–Current–Voltage (P-I-V) characteristics of the VCSEL with 7 µm oxide aperture diameter at different temperatures are shown in Figure 2. The oxide aperture is defined as the length of unoxidized AlAs materials. Continuous-wave (CW) operation in the 10–80 °C temperature range is observed on the fabricated 1130 nm VCSEL. The maximum output power is 3.6 mW at 10 °C and 2.3 mW at 80 °C. A high power output characteristic ensures the integrity of a transmitted signal and extends the transmission distance. The variations in threshold current and slope efficiency with temperature are shown in Figure 3. With the increasing temperature, the threshold current increased first and then decreased. We detuned the gain peak and cavity mode, and there was an offset between the cavity mode and the gain peak at room temperature. With the temperature increase, the gain peak gradually aligns with cavity mode. The lasing mode therefore receives more gain and this results in a lower threshold current. This is a crucial aspect for VCSELs operating at high temperature. At the same time, carriers have more energy at high temperatures, which is proportional to kT (k is Boltzmann constant and T is thermodynamic temperature). Thus, it is easier for the carriers to escape from QWs. This leads to a lower injection efficiency and slope efficiency [15]. Notably, our VCSEL has a slope efficiency of >0.3 W/A even at 80 °C thanks to the offset between gain and cavity mode, which ensures the reliability and stability of operation at high temperatures.

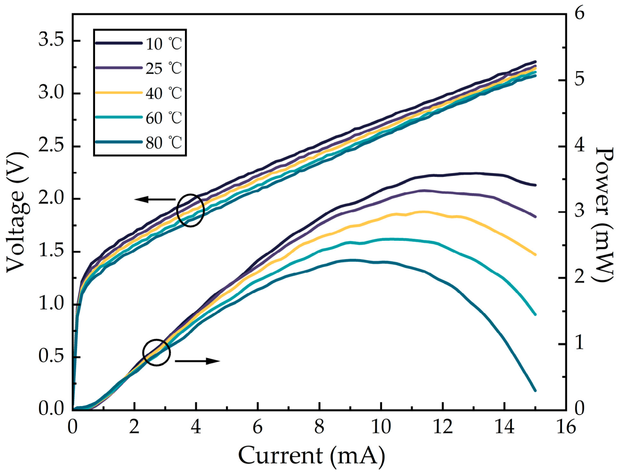

Figure 2. P-I-V characteristics of the 7 μm oxide aperture VCSEL from 10 °C to 80 °C (The black arrows and circles indicate the Y-axis corresponding to the curve, the same as below).

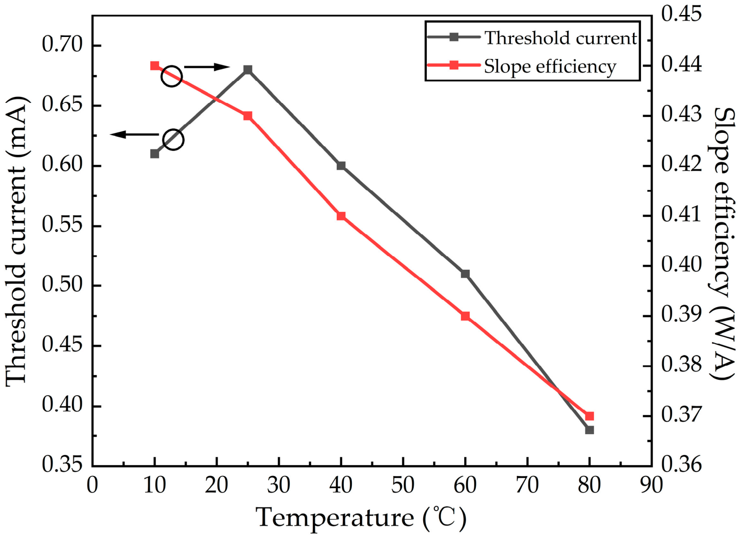

Figure 3. Threshold current and slope efficiency of 7 μm VCSEL at various temperatures.

Figure 4 shows the P-I-V characteristics of the fabricated 1130 nm VCSEL with different oxide aperture diameters. The maximum output power of the 3 μm and 10 μm VCSELs is 1.11 mW and 6.02 mW, respectively. With the increasing oxide aperture, the differential resistance decreases from 420 Ω to 77 Ω. A large oxide aperture leads to a small differential resistance according to ohm law [16]. Figure 5 shows the threshold current density and slope efficiency of different oxide aperture devices. The threshold current density of the 3 μm device is approximately 4.3 kA/cm^2. The high differential resistance and serious Joule heat of the small-aperture device results in a decrease in injection efficiency, and the device enters the thermal roll-off stage earlier. As the oxide aperture increases, the threshold current density decreases and the slope efficiency stays stable. The slope efficiency of the device can be maintained at ~0.44 W/A as the oxide aperture increases from 3 μm to 6 μm, enabling high linearity and output power. The threshold current density is one of the decisive factors for VCSELs to achieve energy-efficient and cost-effective performance. The threshold current density of our device typically ranges from 4.3 kA/cm^2 to 830 A/cm^2.

The low threshold current density can be attributed to the reduced density of states near the valence band maximum due to the strain introduced to QWs by the high In content. It also indicates low optical loss within the cavity and uniform epitaxial quality. The small oxide-aperture device exhibits single-mode operation (shown later) and has a low threshold current (0.3 mA), high output power (1.11 mW) and stable slope efficiency (0.43 W/A). An additional mode control structure is not required, which reduce process complexity while maintaining high output power.

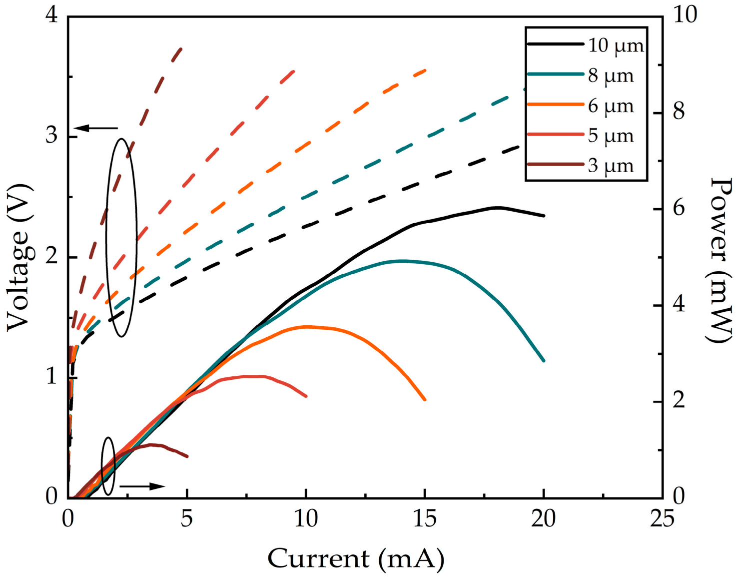

Figure 4. P-I-V characteristics of fabricated 1130 nm VCSELs with different oxide apertures.

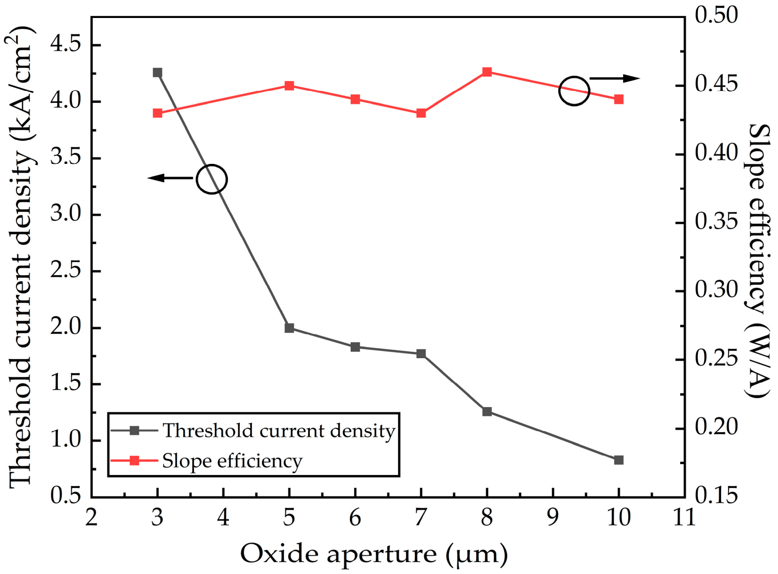

Figure 5. Threshold current density and slope efficiency of different oxide aperture devices.

Figure 6 shows the laser spectrum of a 3 μm oxide aperture device under the bias of I = 2 mA (25 °C) and I = 1.5 mA (80 °C). The device was mounted on a heatsink with a temperature controller, tested by on-wafer probing, and the light from the device was coupled to the multimode fiber directly. The bias current was about $4I_{th}$. The laser spectrum in Figure 6 clearly shows lasing in single transverse mode at a wavelength of 1130 nm. The peak wavelength is measured to be 1128.58 nm at 25 °C. A redshift of approximately Δ = 4.8 nm was observed when the bias current and ambient temperature changed.

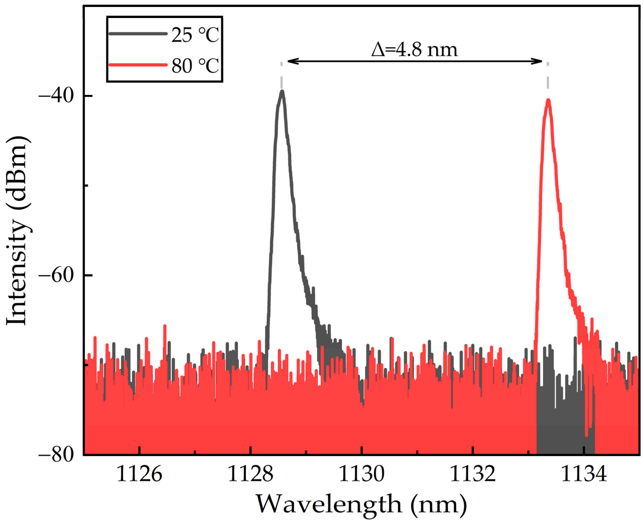

Figure 6. The lasing spectrum of 3 μm VCSEL at two different bias conditions and temperatures: the black curve is I = 2 mA (I/I_{th} = 4) at 25 °C and the red curve is I = 1.5 mA (I/I_{th} = 4) at 80 °C.

Modern short-reach optical interconnection is limited by chromatic dispersion. With the transmission data rate beyond 100 Gb/s, chromatic dispersion is a primary factor in limiting transmitting distance. In addition, high-order transverse modes can lead to the closure of eye diagrams due to their different frequencies compared with fundamental modes. A transmitting distance of 100 m is a target to reach [17]. Recently, some studies evidenced that VCSELs with a narrow optical spectrum enable longer transmission distances at the km scale through multi-mode fibers [18]. The spectral characteristics of VCSELs can be evaluated using the root-mean-square (RMS) spectral width, which can be calculated using an equation [19].

$$\Delta\lambda_{RMS} = \sqrt{\sum_{i=1}^{n} \frac{P_i}{P_{tot}} (\lambda_i - \lambda_{mean})^2} \tag{1}$$

$$\lambda_{mean} = \sum_{i=1}^{n} \frac{P_i}{P_{tot}} \lambda_i \tag{2}$$

where P_i is the power point i of the measured lasing spectrum, P_{tot} is the total power, λ_i is the wavelength point i and λ_{mean} is the mean wavelength.

From Figure 6, the 3 μm oxide aperture device exhibits a clear single mode, where the RMS spectral width is approximately 0.163 nm under the bias of 2 mA at 25 °C and 0.157 nm under the bias of 1.5 mA at 80 °C. The device operates stably in single-mode condition under high bias operation and temperature.

In the field of almost all sensing applications (such as atomic clocks and 3D sensing) and some datacom applications (such as polarization division multiplexing), a stable polarization source is required. For single-mode VCSELs, the emitted light is mainly linearly polarized [20]. In order to characterize the polarization of the VCSEL, a 3 μm device was packaged in the form of TO46 and fixed on the socket. The light emitted by the device was first collimated by a lens, then through a polarizer, and was finally received by the photodetector. The results of OPSR are shown in Figure 7. From Figure 7, the OPSR of 3 μm VCSEL is ~15 dB in the whole operation range. The OPSRs are 13.6 dB and 16.16 dB under the bias currents of 0.8 mA and 5 mA, respectively.

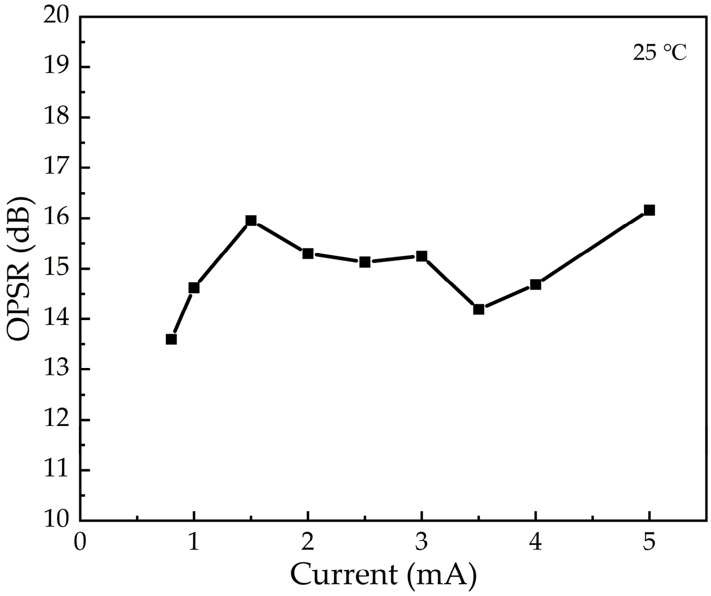

Figure 7. The OPSR of 3 μm VCSEL at 25 °C.

4. VCSEL Small-Signal Analysis

To explore the frequency response characteristics of the fabricated 1130 nm VCSEL, we packaged the device on microstrip line substrate, as shown in Figure 8. Figure 9 shows the typical small-signal response of 3 μm, 5 μm and 7 μm oxide aperture devices measured at 25 °C. As can be seen from Figure 9, the devices exhibit relatively low small-signal responses. For the 3 μm device, the −3 dB bandwidths are 0.16 GHz, 1.32 GHz and 1.14 GHz for the bias currents of 3 mA, 4 mA and 5 mA, respectively. For the 5 μm device, the −3 dB bandwidths are 1.04 GHz, 1.03 GHz and 1.07 GHz for the bias currents of 3 mA, 4 mA and 5 mA, respectively. For the 7 μm device, the −3 dB bandwidths are 2.02 GHz, 1.46 GHz and 1.73 GHz for the bias currents of 3 mA, 4 mA and 5 mA, respectively. The −3 dB bandwidth of the larger-aperture device is better than the small-aperture devices, which might be due to better heat dissipation. A resonance peak is not observed during the response, which indicates there is extreme damping.

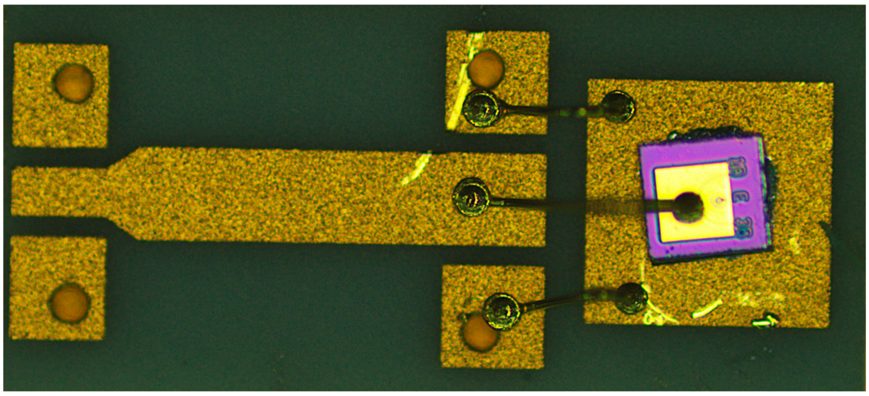

Figure 8. A VCSEL packaged on the microstrip line substrate.

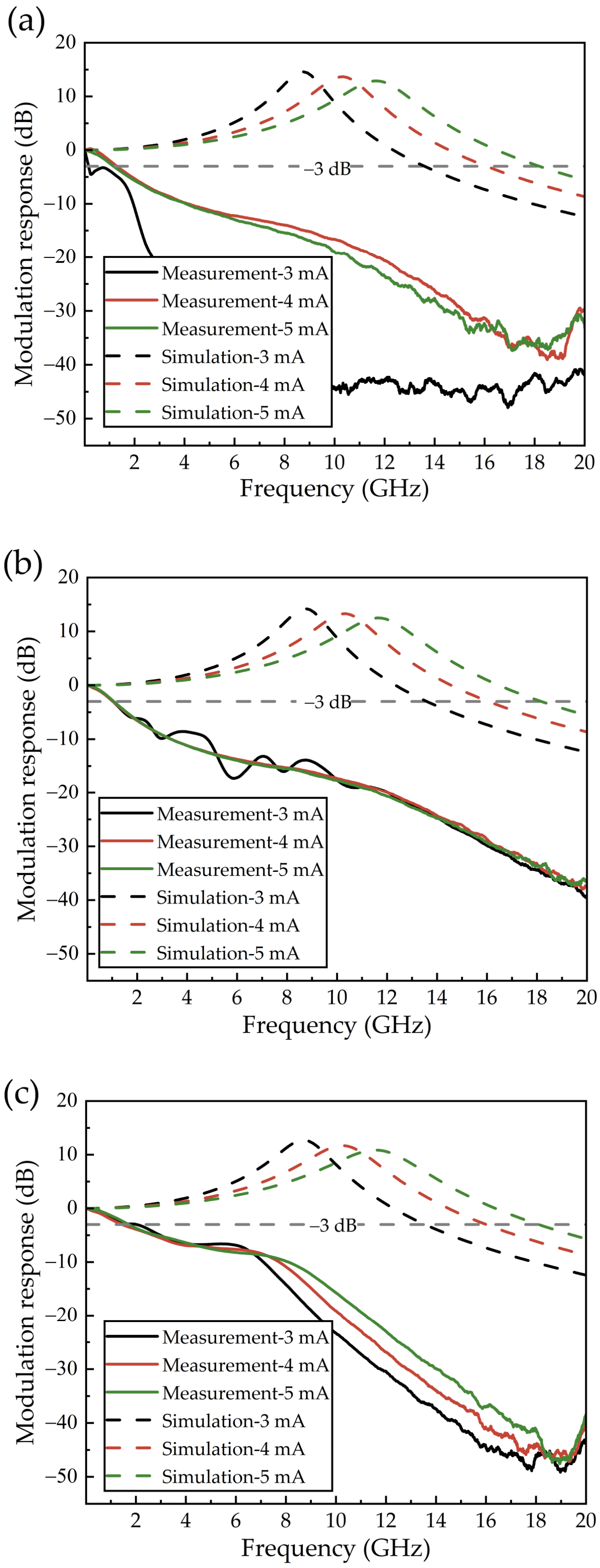

Figure 9. Measured and simulated small-signal modulation response of (**a**) 3 µm, (**b**) 5 µm and (**c**) 7 µm oxide aperture device under different bias currents.

The mechanism limits of modulation response at each bias condition can be described by the three-pole transfer function [21].

$$|H(f)|^2 = \frac{1}{\left[1+\left(\frac{f}{f_o}\right)^2\right]} \cdot \frac{1}{\left[1+\left(\frac{f}{f_r}\right)^2\right] + \left(\frac{\gamma}{2\pi f_r}\right)^2 \left(\frac{f}{f_r}\right)^2} \quad (3)$$

where f_o is the parasitic cut-off frequency and γ is the damping frequency.

The first term of Equation (3) models the electrical chip parasitics by a single parasitic pole. The second term of Equation (3) can be directly derived by small-signal analysis of the rate equations above the threshold. During the fabrication of our 1130 nm VCSEL, the coplanar waveguide pads process was not adopted in the device [22,23]. For the convenience of the response test, devices with off-plane electrodes were packaged on the microstrip line. This also induced the effects of transmission line and impedance mismatch, resulting in reduced bandwidth. Apart from the influences of parasitic components, the intrinsic response of the VCSEL can be described by the rate equation model [24].

$$\frac{dN}{dt} = \frac{\eta_i}{qV_{act}} - R_{sp} - v_g g N_p \quad (4)$$

$$\frac{dN_p}{dt} = R'_{sp} + \Gamma v_g g N_p - \frac{N_p}{\tau_p} \quad (5)$$

where N is the carrier density, N_p is the photon density, η_i is the internal quantum efficiency, q is the electron charge, V_{act} is the active region volume, R_{sp} is the carrier recombination rate, R'_{sp} is the coupled recombination rate, v_g is the group velocity, g is the differential gain, Γ is the mode confinement factor and τ_p is the photon lifetime. For the multi-mode case, the standard single-mode rate equation model can be expanded to a carrier–source reservoir, which supplies multiple photon reservoirs.

The -3 dB bandwidth of a VCSEL is proportional to the relaxation frequency. The analysis of the rate equation leads to the following expression for the relaxation frequency of a single-mode semiconductor laser [24]:

$$f_r = \frac{1}{2\pi}\sqrt{\frac{v_g \eta_i g}{qV_p}(I - I_{th})} \quad (6)$$

where V_p is the effective mode volume, I is the bias current and I_{th} is the threshold current.

The model-projected curves of intrinsic response are also plotted in Figure 9. The numerical values of the laser parameters listed in Table 1 are used.

Table 1. Definition and numerical values of the VCSEL parameters.

Parameter (Unit)	Symbol	Value
Group velocity (cm/s)	v_g	1×10^{10}
Quantum efficiency	η_i	0.8
Internal losses (cm^{-1})	α_i	20
Confinement factor	Γ	0.0057
Photon lifetime (ps)	τ_p	2.5×10^{-12}
Differential gain (cm^2)	g	19.3×10^{-16}

From Figure 9, with the consideration of intrinsic dynamics modulation, the -3 dB optical modulation bandwidth for the 3 µm VCSEL is expected to reach 13.61 GHz, 16.07 GHz and 18.19 GHz for the bias currents of 3 mA, 4 mA and 5 mA, respectively. For the 5 µm VCSEL, the -3 dB intrinsic bandwidth is expected to reach 13.59 GHz, 16.04 GHz and 18.16 GHz for the bias currents of 3 mA, 4 mA and 5 mA, respectively. For the 7 µm VCSEL, the -3 dB intrinsic bandwidth is expected to reach 13.56 GHz, 16.01 GHz and

18.11 GHz for the bias currents of 3 mA, 4 mA and 5 mA, respectively. Reducing the parasitic effect can improve the overall response of the device. In future research, the improved high-speed device process will be applied to package the VCSEL to reduce the impact of parasitic effects on dynamic response. With a more refined structure layout and process, the optical dynamics response characteristics of the device can be further improved later.

5. Conclusions

In conclusion, we have demonstrated a 1130 nm InGaAs VCSEL grown by MOCVD. The output power of the 7 μm oxide aperture device reaches 3.06 mW at 10 °C and 1.54 mW at 80 °C. The threshold current is 0.68 mA at 25 °C and 0.38 mA at 80 °C, corresponding to threshold current densities of 1.7 kA/cm^2 and 0.9 kA/cm^2, respectively. The slope efficiency is 0.44 W/A at 10 °C and 0.37 W/A at 80 °C. When the oxide aperture diameter increases from 3 μm to 10 μm, the threshold current density decreases from 4.26 kA/cm^2 to 830 A/cm^2 and the slope efficiency remains stable (~0.44 W/A), which is beneficial to the reliable operation and high linearity output of the device. The maximum output power of the 3 μm and 10 μm VCSELs is 1.11 mW and 6.02 mW, respectively. The 3 μm aperture device shows lasing in single transverse mode at a wavelength of 1128.58 nm at 25 °C and the OPSR is ~15 dB. A redshift of approximately Δ = 4.8 nm was observed when the bias current and temperature changed. From the results, a single-mode VCSEL with low-threshold and high-output characteristics was achieved by simply reducing the oxide aperture, which matches the standard VCSEL process and future development direction. In our experiments, the modulation responses of the 3 μm, 5 μm and 7 μm devices are relatively low, which might be due to the off-plane electrode process and the devices being packaged on the microstrip line substrate. From the results of intrinsic response, we suggest that the optimized process structure and package method should be adopted to increase the modulation response; this will be our future work.

These results show a possibility of achieving a long-wavelength InGaAs VCSEL with low threshold current density and high efficiency and output power. Further optimizations can be expected to achieve improved dynamic response characteristics and narrower spectral width to make our device a viable solution for silicon photonics.

Author Contributions: Conceptualization, Y.F. and Y.Z.; methodology, Y.F. and Y.Z.; software, Y.F.; formal analysis, Y.F. and Y.Z.; investigation, Y.F. and C.L.; data curation, Y.F., Y.Z., C.L., J.L. and Y.W.; writing—original draft preparation, Y.F.; writing—review and editing, Y.Z. and X.W.; supervision, X.W.; project administration, X.W.; funding acquisition, X.W. All authors have read and agreed to the published version of the manuscript.

Funding: This research was funded by the National Natural Science Foundation of China, grant number 62004190, and the National Key Research and Development Program of China, grant number 2018YFE0203103.

Institutional Review Board Statement: Not applicable.

Informed Consent Statement: Not applicable.

Data Availability Statement: The data presented in this study are available on request from the corresponding author. The data are not publicly available as the data also form part of an ongoing study.

Conflicts of Interest: The authors declare no conflicts of interest.

References

1. Chowdhury, M.Z.; Shahjalal, M.; Ahmed, S.; Jang, Y.M. 6G Wireless Communication Systems: Applications, Requirements, Technologies, Challenges, and Research Directions. *IEEE Open J. Commun. Soc.* **2020**, *1*, 957–975. [CrossRef]
2. Yu, H.; Pantouvaki, M.; Verheyen, P.; Lepage, G.; Absil, P.; Bogaerts, W.; Van Campenhout, J. Silicon dual-ring modulator driven by differential signal. *Opt. Lett.* **2014**, *39*, 6379–6382. [CrossRef]

3. Green, W.M.J.; Rooks, M.J.; Sekaric, L.; Vlasov, Y.A. Ultra-compact, low RF power, 10 Gb/s silicon Mach-Zehnder modulator. *Opt. Express* **2007**, *15*, 17106–17113. [CrossRef] [PubMed]
4. Feng, N.-N.; Liao, S.; Feng, D.; Dong, P.; Zheng, D.; Liang, H.; Shafiiha, R.; Li, G.; Cunningham, J.E.; Krishnamoorthy, A.V.; et al. High speed carrier-depletion modulators with 1.4 V-cm V π L integrated on 0.25 µm silicon-on-insulator waveguides. *Opt. Express* **2010**, *18*, 7994–7999. [CrossRef]
5. Gostimirovic, D.; Ye, W.N. Compact silicon-photonic mode-division (de)multiplexer using waveguide-wrapped microdisk resonators. *Opt. Lett.* **2021**, *46*, 388–391. [CrossRef] [PubMed]
6. Munk, D.; Katzman, M.; Kaganovskii, Y.; Inbar, N.; Misra, A.; Hen, M.; Priel, M.; Feldberg, M.; Tkachev, M.; Bergman, A.; et al. Eight-Channel Silicon-Photonic Wavelength Division Multiplexer With 17 GHz Spacing. *IEEE J. Sel. Top. Quantum Electron.* **2019**, *25*, 1–10. [CrossRef]
7. Ding, Y.; Ou, H.; Xu, J.; Peucheret, C. Silicon Photonic Integrated Circuit Mode Multiplexer. *IEEE Photon-Technol. Lett.* **2013**, *25*, 648–651. [CrossRef]
8. Liu, A.; Liao, L.; Chetrit, Y.; Basak, J.; Nguyen, H.; Rubin, D.; Paniccia, M. Wavelength Division Multiplexing Based Photonic Integrated Circuits on Silicon-on-Insulator Platform. *IEEE J. Sel. Top. Quantum Electron.* **2009**, *16*, 23–32.
9. Dehlinger, G.; Koester, S.; Schaub, J.; Chu, J.; Ouyang, Q.; Grill, A. High-Speed Germanium-on-SOI Lateral PIN Photodiodes. *IEEE Photonics Technol. Lett.* **2004**, *16*, 2547–2549. [CrossRef]
10. Going, R.; Seok, T.J.; Loo, J.; Hsu, K.; Wu, M.C. Germanium wrap-around photodetectors on Silicon photonics. *Opt. Express* **2015**, *23*, 11975–11984. [CrossRef]
11. Shi, Y.; Zhang, Y.; Wan, Y.; Yu, Y.; Zhang, Y.; Hu, X.; Xiao, X.; Xu, H.; Zhang, L.; Pan, B. Silicon photonics for high-capacity data communications. *Photonics Res.* **2022**, *10*, A106–A134. [CrossRef]
12. Kondo, T.; Arai, M.; Azuchi, M.; Uchida, T.; Matsutani, A.; Miyamoto, T.; Koyama, F. Low threshold current density operation of 1.16 µm highly strained GaInAs/GaAs vertical cavity surface emitting lasers on (100) GaAs substrate. *Jpn. J. Appl. Phys.* **2002**, *41*, L562. [CrossRef]
13. Grenouillet, L.; Duvaut, P.; Olivier, N.; Gilet, P.; Grosse, P.; Poncet, S.; Philippe, P.; Pougeoise, E.; Fulbert, L.; Chelnokov, A. GaIn (N) As/GaAs VCSELs emitting in the 1.1-1.3 µm range[C]//Workshop on Optical Components for Broadband Communication. *SPIE* **2006**, *6350*, 86–93.
14. Stevens, R.; Gilet, P.; Larrue, A.; Grenouillet, L.; Olivier, N.; Grosse, P.; Gilbert, K.; Teysseyre, R.; Chelnokov, A. Singlemode 1.1 µm InGaAs quantum well microstructured photonic crystal VCSEL[C]//Vertical-Cavity Surface-Emitting Lasers XII. *SPIE* **2008**, *6908*, 106–115.
15. Schäfer, F.; Mayer, B.; Reithmaier, J.P.; Forchel, A. High-temperature properties of GaInAs/AlGaAs lasers with improved carrier confinement by short-period superlattice quantum well barriers. *Appl. Phys. Lett.* **1998**, *73*, 2863–2865. [CrossRef]
16. MacDougal, M.; Geske, J.; Lin, C.-K.; Bond, A.; Dapkus, P. Low resistance intracavity-contacted oxide-aperture VCSELs. *IEEE Photonics Technol. Lett.* **1998**, *10*, 9–11. [CrossRef]
17. Castro, J.M.; Pimpinella, R.; Kose, B.; Huang, P.; Novick, A.; Lane, B. Modal-Chromatic dispersion interaction effects for 850 nm VCSEL channels at 100 Gb/s per wavelength. *J. Light. Technol.* **2020**, *39*, 2067–2076. [CrossRef]
18. Ledentsov, N.; Chorchos, L.; Makarov, O.; Kropp, J.-R. Narrow spectrum VCSEL development for high performance 100G transceivers and increased transmission distance over multimode fiber[C]//Vertical-Cavity Surface-Emitting Lasers XXV. *SPIE* **2021**, *11704*, 78–84.
19. Haglund, E.; Haglund, Å.; Gustavsson, J.S.; Kögel, B. Reducing the spectral width of high speed oxide confined VCSELs using an integrated mode filter[C]//Vertical-Cavity Surface-Emitting Lasers XVI. *SPIE* **2012**, *8276*, 171–178.
20. Ostermann, J.M.; Michalzik, R. *Polarization Control of VCSELs[M]//VCSELs: Fundamentals, Technology and Applications of Vertical-Cavity Surface-Emitting Lasers*; Springer: Berlin/Heidelberg, Germany, 2012; pp. 147–179.
21. Thibeault, B.; Bertilsson, K.; Hegblom, E.; Strzelecka, E.; Floyd, P.; Naone, R.; Coldren, L. High-speed characteristics of low-optical loss oxide-apertured vertical-cavity lasers. *IEEE Photonics Technol. Lett.* **1997**, *9*, 11–13. [CrossRef]
22. Al-Omari, A.N.; Al-Kofahi, I.K.; Lear, K.L. Fabrication, performance and parasitic parameter extraction of 850 nm high-speed vertical-cavity lasers. *Semicond. Sci. Technol.* **2009**, *24*, 095024. [CrossRef]
23. Chang, Y.C.; Coldren, L.A. Efficient, high-data-rate, tapered oxide-aperture vertical-cavity surface-emitting lasers. *IEEE J. Sel. Top. Quantum Electron.* **2009**, *15*, 704–715. [CrossRef]
24. Coldren, L.A.; Corzine, S.W.; Mashanovitch, M.L. *Diode Lasers and Photonic Integrated Circuits*; John Wiley & Sons: Hoboken, NJ, USA, 2012.